Small-Signal State-Space Analysis of Inductive Battery Charging System in Off-Resonant Operation

Ernst Torsgård[1]
[1] Dept. Engineering Cybernetics
NTNU
Trondheim, Norway
ernstt@stud.ntnu.no

Giuseppe Guidi[2]
[2] SINTEF Energy Research
Trondheim, Norway
Giuseppe.Guidi@sintef.no

Jon Are Suul[1,2]
[1] Dept. Engineering Cybernetics
NTNU
Trondheim, Norway
jon.are.suul@ntnu.no

***Abstract*—This paper analyses the small-signal dynamics of a series-series compensated inductive charging system with a passive diode rectifier interfaced directly to a battery on the receiving side. The analyzed system is designed for utilizing the constant voltage load (CVL) characteristics of the battery to enable power flow control at constant input/output voltages by changing the frequency in response to variations in coupling conditions. A linearizable state-space model, including the nonlinear CVL characteristics, is presented and utilized to evaluate the small-signal dynamics of the studied system. Eigenvalue trajectories and frequency characteristics are presented to show how the small-signal dynamics vary with the coupling conditions and how this will influence controller tuning requirements. Time-domain simulations are presented to verify the validity of the small-signal modelling and to demonstrate the performance of sub-resonant frequency control by a simple PI-controller regulating the power flow in response to variations in the coupling conditions.**

***Index Terms*—Eigenvalue Analysis, Inductive Power Transfer, Nonlinear Time-Invariant State-Space Model, Off-Resonant Operation of Inductive Charging System, Small-Signal Analysis**

I. Introduction

Inductive power transfer (IPT) technology is currently being widely studied for wireless battery charging of electric vehicles (EVs) [1], [2], [3]. The functionality and operating frequency of such systems are currently being standardized for resonant operation within a narrow frequency band [4]. However, IPT system designs and control strategies relying on variable frequency control have also been proposed [5], and can still be relevant for applications that are not standardized for operation in a narrow frequency range. In addition to specially engineered or customized systems, variable frequency control can, for instance, be relevant for subsea charging systems, [6] or marine transport applications [7], [8].

Most proposed strategies for frequency control of resonant IPT systems are based on increasing the operating frequency when the magnetic coupling is reduced [5]. The system must then be designed so that the power flow at a constant input voltage amplitude is decreased when the frequency is increased beyond the resonance frequency. Thus, such systems are typically designed to operate at resonance with maximum sending side voltage at the highest expected coupling. Frequency control, or dual voltage-frequency control, in the super-resonant region can then be applied for regulating the power flow at lower coupling [5].

A different approach for design and control of series-series (SS) compensated IPT systems intended for off-resonant operation was introduced in [7], [9], [10]. By this approach, the system should be designed for resonant operation with rated input voltage at the minimum coupling condition. The design approach takes advantage of the constant voltage load (CVL) characteristics resulting from a diode rectifier directly interfaced to a battery for enhancing the off-resonant power transfer capability. Thus, the system is operated in the bifurcated region when the magnetic coupling is above the minimum value where the system is designed for rated power flow. This design approach can enable off-resonant control for regulating the power flow over a wide range of coupling conditions with constant input and output voltages, ensuring minimized current rating requirements for the system components [10]. As discussed in [9], [10] designs for power control by sub-resonant operation should be preferred, since this can ensure slightly inductive operation and minimized switching losses for the sending side converter. However, the design approach and the analysis presented in [10] were only based on the steady-state frequency characteristics of the system.

This paper presents a linearizable state-space model of an SS compensated IPT system designed according to the approach from [9], [10], for analyzing the small-signal dynamics and the controller tuning for variable frequency operation. The presented model includes the nonlinearity due to the CVL characteristics of battery charging and allows for accurate assessment of the small-signal dynamics at off-resonant operation over a defined range of variations in the operating conditions. The accuracy of the presented model is verified by time-domain simulations. Furthermore, the eigenvalues and frequency-domain characteristics of the small-signal model are evaluated along the trajectory corresponding to a constant rated power transfer over the full range of expected coupling conditions. The results are utilized to design a simple PI-

The work of SINTEF Energy Research in this paper was supported by the Internal Strategic Institute Project "Innovative Power Transfer Transfer Technology for Electric Transportation (IPT-ElTra) financed by the national Basic Funding Scheme of Norway.

978-1-7281-1842-0/19/$31.00

This is the accepted version of a paper published in 2019 20th Workshop on Control and Modeling for Power Electronics - COMPEL
DOI: 10.1109/COMPEL.2019.8769678

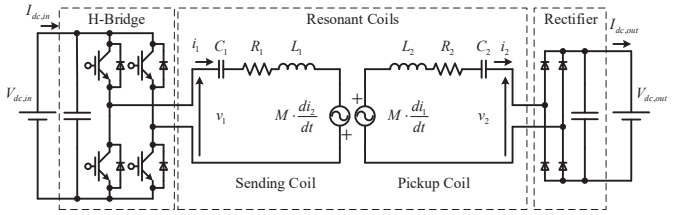

Fig. 1. Series-series compensated IPT system with constant voltage load

controller for regulating the power transfer for battery charging in response to variations in operating conditions.

II. Design of SS Compensated IPT Systems for Off-Resonant Operation with CVL

The studied configuration is an SS compensated IPT system, as shown in Fig. 1, with an H-bridge converter on the sending side and a diode rectifier interfaced directly to a battery on the receiving side, as represented by a voltage source.

A. Dynamic model with time-periodic variables

The state equations for the configuration in Fig. 1 can be expressed directly from the circuit diagram as:

$$\begin{cases} v_1 = v_{C1} + R_1 i_1 + L_1 \dfrac{di_1}{dt} - M\dfrac{di_2}{dt} \\ v_2 = M\dfrac{di_1}{dt} - L_2\dfrac{di_2}{dt} - R_2 i_2 - v_{C2} \\ \dfrac{dv_{C_1}}{dt} = \dfrac{1}{C_1} i_1 \\ \dfrac{dv_{C_2}}{dt} = \dfrac{1}{C_2} i_2 \end{cases} \tag{1}$$

Assuming sinusoidal currents and introducing a first harmonic approximation of the voltage v_2 at the terminals of the diode rectifier, the CVL characteristics can be modelled by:

$$v_2 = \frac{i_2}{I_2} \cdot \frac{4}{\pi} \cdot V_{dc,out} \tag{2}$$

In this equation I_2 represents the amplitude of i_2. Thus, the amplitude of the first harmonic voltage component at the receiving side is determined by the dc output voltage while the characteristics of the diode rectifier impose that the voltage will be in phase with the receiving side current. As will be shown in the following, the nonlinearity introduced by the constant dc voltage in combination with the diode rectifier significantly influences the frequency characteristics and the small-signal dynamics of the system.

B. Frequency characteristics of CVL IPT systems with impact of unbalancing and detuning

Representing the fundamental frequency currents and voltages in (1) and (2) by phasor variables, it is possible to derive the steady-state frequency characteristics (i.e. with $d/dt = j\omega$) of the power transfer capability of the studied system with CVL characteristics, as explained in [10]. The power transfer capability and phase angle of the equivalent impedance for an ideal lossless case is given by the black curves in Fig. 2.

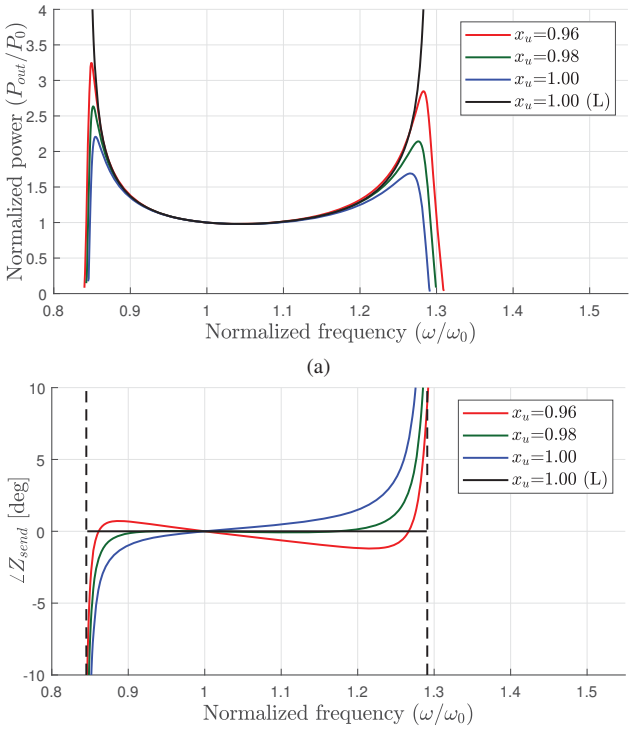

Fig. 2. Effect of unbalancing: "L" denotes a lossless system , coils with coupling factor $k = \frac{M}{\sqrt{L_1 L_2}} = 0.4$, $\omega_0 = \frac{1}{\sqrt{C_1 L_1}} = \frac{1}{\sqrt{C_2 L_2}}$, $Q_1 = 310$ and $Q_2 = 270$. Power is normalized to $P_0 = P(k, x_u, x_c, \omega_0)$.

These curves show that the power transfer capability with CVL characteristics are ideally approaching infinite when reducing or increasing the frequency from the resonance frequency, while the phase angle of the equivalent impedance is zero in the full range of feasible operating conditions. In a practical circuit, the losses will limit the maximum power transfer capability as shown by the blue curve in Fig. 2a. Still, the figure shows how the CVL characteristics will cause two pronounced peaks in the power transfer and Fig. 2b shows that the phase angle of the equivalent impedance will be close to zero in a large share of the frequency range between these two peaks.

In [9] and [10], it is shown how the off-resonant peaks in the power transfer characteristics of a system with CVL characteristics can be enhanced by introducing an unbalance factor x_u defined by:

$$x_u^2 \cdot \frac{L_2}{L_1} = \left(\frac{V_2}{V_1}\right)^2, \quad 0 < x_u \leq 1 \tag{3}$$

The result of reducing x_u is shown by the green and red curves in in Fig. 2. As demonstrated by Fig. 2a, unbalancing of the voltage or inductance ratios can be utilized to enhance the off-resonant peaks in the power transfer capability. The curves in Fig. 2b also show how unbalancing enhances the bifurcation in the phase characteristics.

To further shape the frequency characteristics, a detuning factor x_c, [10], can be introduced as given by (4):

This is the accepted version of a paper published in 2019 20th Workshop on Control and Modeling for Power Electronics - COMPEL
DOI: 10.1109/COMPEL.2019.8769678

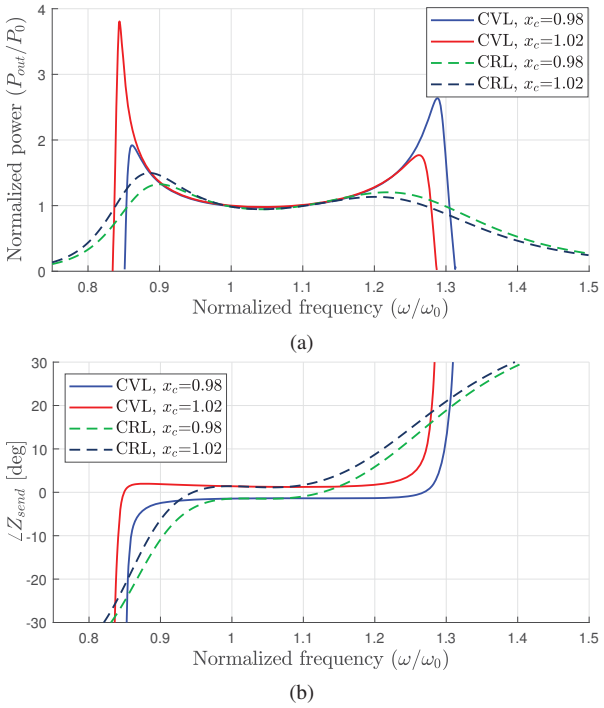

Fig. 3. Effect of detuning and comparison between CVL and CRL. Coils with coupling factor $k = 0.4$ as in Fig. 2 and unbalance factor $x_u = 0.98$. Power is normalized to $P_0 = P(k, x_u, x_c, \omega_0)$.

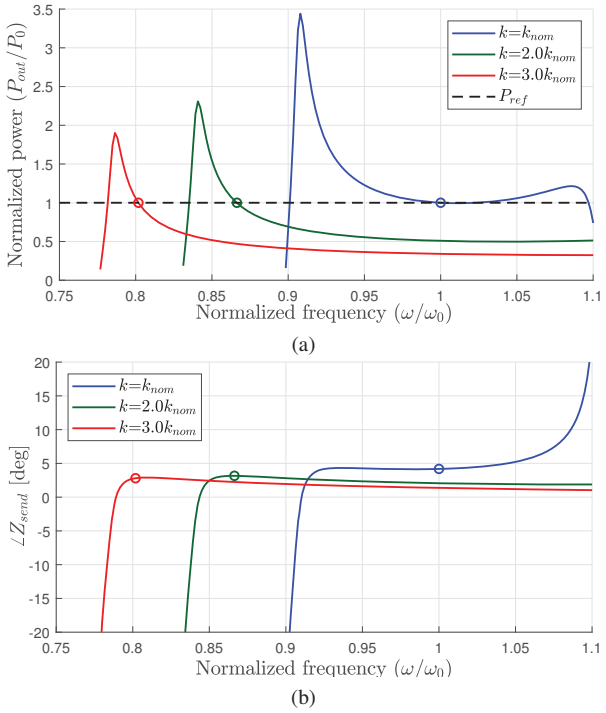

Fig. 4. Operation with constant power transfer at variable coupling: operating points marked with a circle. Coils with unbalance factor $x_u = 0.98$, detuning factor $x_c = 1.03$, nominal coupling factor $k_{nom} = 0.2$. Power normalized to $P_0 = P(k_{nom}, x_u, x_c, \omega_0)$.

$$x_c = \frac{C_1 \cdot L_1}{C_2 \cdot L_2} \tag{4}$$

As a result of such detuning, the system will no longer have a single defined resonance frequency, i.e. $\omega_0 = \omega_{2,0} = \frac{1}{\sqrt{C_2 L_2}} \neq \frac{1}{\sqrt{C_1 L_1}} = \omega_{1,0}$. By selecting values for x_c above or below 1.0, either the sub- or super-resonant peak in power transfer characteristics, respectively, can be enhanced. Fig. 3 shows how this affects the frequency characteristics of a system with CVL compared to a case with a constant resistive load (CRL). Clearly, a small amount of detuning will more strongly enhance the sub- or super-resonant power peaks in the CVL case than for the CRL case. Furthermore, the effect of detuning on the phase characteristics is shown in Fig. 3b. This figure shows how a detuning factor of $x_c > 1$ ensures a slightly inductive sending side impedance over the whole frequency range of interest, whereas a factor of $x_c < 1$ implies a slightly capacitive impedance. The figure also shows that the CVL leads to an almost constant phase angle close to zero in a much wider frequency range than for the CRL.

C. Off-resonant operation for power flow control

The introduction of unbalancing and detuning of the SS IPT system with CVL allows for maintaining high power transfer capability in a wide range of coupling conditions by utilizing off-resonant operation. Thus, the power transfer can be kept constant by regulating the operating frequency in response to changes in the coupling conditions [10]. An example of such operation is illustrated by the frequency characteristics

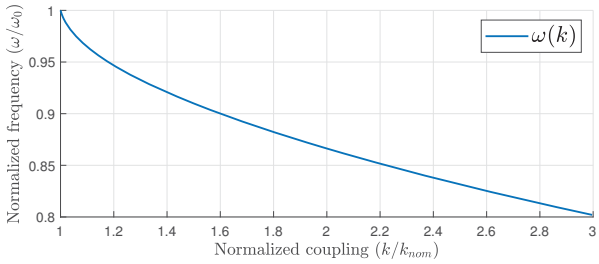

Fig. 5. Required operating frequency as function of coupling factor for maintaining constant power transfer with sub-resonant frequency control.

of the IPT system for three different values of k in Fig. 4. As indicated by Fig. 4b, the equivalent sending side impedance will remain slightly inductive over the whole frequency range, which will help to minimize switching losses of the sending side H-bridge converter. Since the operating strategy given by Fig. 4 is obtained with constant input and output voltage and a phase angle of the sending side equivalent impedance close to zero, the current amplitude will also remain almost constant over the full range of expected operating conditions. Thus, contrary to systems operating at the resonance frequency, IPT systems designed and controlled according to the approach from [9], [10] avoids the need for increasing the current rating of components proportionally to the expected variations in the coupling coefficient.

The required variations in the frequency as a function of the coupling conditions are shown in Fig. 5. It can be noticed from Fig. 4a and Fig. 5 that the sensitivity of the power flow

This is the accepted version of a paper published in 2019 20th Workshop on Control and Modeling for Power Electronics - COMPEL
DOI: 10.1109/COMPEL.2019.8769678

to the frequency will change significantly with the coupling conditions. Thus, it will be important to evaluate the small-signal dynamics of the system for designing a suitable control loop to regulate the power flow by changing the frequency.

III. Time-Invariant State-Space Modelling of SS Compensated ITP Systems with CVL

For utilizing state-space modelling techniques to analyze the small-signal characteristics of the studied system, a time-invariant and linearizable model is needed. Such models can be obtained by dq-frame representation or dynamic phasor-based modeling [11]. Such modelling approaches have been studied for various IPT systems, for instance by [12], [13], [14], [15]. However, the following analysis will specifically address the nonlinearity of CVL characteristics and the off-resonant operation according to Fig. 4 and Fig. 5.

A. Nonlinear state-space model

As mentioned, CVL characteristics introduce nonlinearity in the receiving side. Assuming a dq-frame representation of the state variables in a first harmonic approximation, the nonlinearity from (2) can be represented by (5) [16]:

$$v_{2,dq} = \frac{i_{2,dq}}{|i_{2,dq}|} \cdot \frac{4}{\pi} \cdot V_{dc,out} = \frac{i_{2,dq}}{\sqrt{i_{2,d}^2 + i_{2,q}^2}} \cdot \frac{4}{\pi} \cdot V_{dc,out} \quad (5)$$

Thus, a nonlinear model can be derived by dq-frame representation of all state variables from (1), and can be expressed on the general state-space form given by:

$$\dot{\boldsymbol{x}} = \boldsymbol{f}(\boldsymbol{x}, \boldsymbol{u}), \quad \boldsymbol{y} = \boldsymbol{g}(\boldsymbol{x}, \boldsymbol{u}) \quad (6)$$

with the states $\boldsymbol{x}$, input signals $\boldsymbol{u}$ and output $\boldsymbol{y}$ defined by:

$$\begin{aligned} \boldsymbol{x} &= \begin{bmatrix} i_{1,d} & i_{1,q} & i_{2,d} & i_{2,q} & v_{C1,d} & v_{C1,q} & v_{C2,d} & v_{C2,q} \end{bmatrix}^T \\ \boldsymbol{u} &= \begin{bmatrix} v_{1,d} & v_{1,q} & \omega & V_{dc,out} \end{bmatrix}^T \\ \boldsymbol{y} &= \begin{bmatrix} P_{in} \\ P_{out} \end{bmatrix} = \begin{bmatrix} v_{1,d} \cdot i_{1,d} + v_{1,q} \cdot i_{1,q} \\ v_{2,d} \cdot i_{2,d} + v_{2,q} \cdot i_{2,q} \end{bmatrix} \end{aligned} \quad (7)$$

Introducing the leakage factors $L_{\alpha1} = L_1 - M^2/L_2$ and $L_{\alpha2} = L_2 - M^2/L_1$, the resulting nonlinear state-space model can be derived as given by (8). This model can be linearized at any equilibrium point corresponding to a feasible operating condition of the system. Accordingly, the small-signal dynamics around the steady-state operating point defined by $\boldsymbol{f}(\boldsymbol{x_0}, \boldsymbol{u_0}) = \boldsymbol{0}$ can be studied by evaluating the eigenvalues of the $\boldsymbol{A}$-matrix when the system is expressed on the general linearized state-space form according to (9). The $\boldsymbol{A}, \boldsymbol{B}$ and $\boldsymbol{C}$ matrices resulting from linearization of the studied system can be expressed by (10), (11) and (12), respectively. The elements $A_{i,j}$ and $B_{i,j}$ in (10) and (11) are given by (13). For these expressions, dq-subscripts indicate that $i_{2,d,0}$ and $i_{2,q,0}$ should be used in the first and second element, respectively, and the $\pm$-sign indicates a positive and negative value for the corresponding first and second matrix entry.

$$\begin{aligned}
\frac{di_{1,d}}{dt} &= \omega \cdot i_{1,q} - \frac{R_1}{L_{\alpha1}} \cdot i_{1,d} - \frac{MR_2}{L_{\alpha1}L_2} \cdot i_{2,d} - \frac{1}{L_{\alpha1}} \cdot v_{C1,d} \\
&- \frac{M}{L_{\alpha1}L_2} \cdot v_{C2,d} + \frac{1}{L_{\alpha1}} \cdot v_{1,d} - \frac{M}{L_{\alpha1}L_2} \cdot \frac{i_{2,d}}{\sqrt{i_{2,d}^2 + i_{2,q}^2}} \cdot \frac{4}{\pi} \cdot V_{dc,out} \\
\frac{di_{1,q}}{dt} &= -\omega \cdot i_{1,d} - \frac{R_1}{L_{\alpha1}} \cdot i_{1,q} - \frac{MR_2}{L_{\alpha1}L_2} \cdot i_{2,q} - \frac{1}{L_{\alpha1}} \cdot v_{C1,q} \\
&- \frac{M}{L_{\alpha1}L_2} \cdot v_{C2,q} + \frac{1}{L_{\alpha1}} \cdot v_{1,q} - \frac{M}{L_{\alpha1}L_2} \cdot \frac{i_{2,q}}{\sqrt{i_{2,d}^2 + i_{2,q}^2}} \cdot \frac{4}{\pi} \cdot V_{dc,out} \\
\frac{di_{2,d}}{dt} &= \omega \cdot i_{2,q} - \frac{MR_1}{L_{\alpha2}L_1} \cdot i_{1,d} - \frac{R_2}{L_{\alpha2}} \cdot i_{2,d} - \frac{M}{L_{\alpha2}L_1} \cdot v_{C1,d} \\
&- \frac{1}{L_{\alpha2}} \cdot v_{C2,d} + \frac{M}{L_{\alpha2}L_1} \cdot v_{1,d} - \frac{1}{L_{\alpha2}} \cdot \frac{i_{2,d}}{\sqrt{i_{2,d}^2 + i_{2,q}^2}} \cdot \frac{4}{\pi} \cdot V_{dc,out} \\
\frac{di_{2,q}}{dt} &= -\omega \cdot i_{2,d} - \frac{MR_1}{L_{\alpha2}L_1} \cdot i_{1,q} - \frac{R_2}{L_{\alpha2}} \cdot i_{2,q} - \frac{M}{L_{\alpha2}L_1} \cdot v_{C1,q} \\
&- \frac{1}{L_{\alpha2}} \cdot v_{C2,q} + \frac{M}{L_{\alpha2}L_1} \cdot v_{1,q} - \frac{1}{L_{\alpha2}} \cdot \frac{i_{2,q}}{\sqrt{i_{2,d}^2 + i_{2,q}^2}} \cdot \frac{4}{\pi} \cdot V_{dc,out} \\
\frac{dv_{C1,d}}{dt} &= \omega \cdot v_{C1,q} + \frac{1}{C_1} \cdot i_{1,d} \\
\frac{dv_{C1,q}}{dt} &= -\omega \cdot v_{C1,d} + \frac{1}{C_1} \cdot i_{1,q} \\
\frac{dv_{C2,d}}{dt} &= \omega \cdot v_{C2,q} + \frac{1}{C_2} \cdot i_{2,d} \\
\frac{dv_{C2,q}}{dt} &= -\omega \cdot v_{C2,d} + \frac{1}{C_2} \cdot i_{2,q}
\end{aligned} \quad (8)$$

$$\begin{aligned} \Delta\dot{\boldsymbol{x}} &= \boldsymbol{A}(\boldsymbol{x}_0, \boldsymbol{u}_0) \cdot \Delta\boldsymbol{x} + \boldsymbol{B}(\boldsymbol{x}_0, \boldsymbol{u}_0) \cdot \Delta\boldsymbol{u} \\ \Delta\boldsymbol{y} &= \boldsymbol{C}(\boldsymbol{x}_0, \boldsymbol{u}_0) \cdot \Delta\boldsymbol{x} \end{aligned} \quad (9)$$

$$\boldsymbol{A} = \begin{bmatrix} \frac{-R_1}{L_{\alpha1}} & \omega_0 & A_{1,3} & A_{1,4} & \frac{-1}{L_{\alpha1}} & 0 & \frac{-M}{L_{\alpha1}L_2} & 0 \\ -\omega_0 & \frac{-R_1}{L_{\alpha1}} & A_{2,3} & A_{2,4} & 0 & \frac{-1}{L_{\alpha1}} & 0 & \frac{-M}{L_{\alpha1}L_2} \\ \frac{-MR_1}{L_{\alpha2}L_1} & 0 & A_{3,3} & A_{3,4} & \frac{-M}{L_{\alpha2}L_1} & 0 & \frac{-1}{L_{\alpha2}} & 0 \\ 0 & \frac{-MR_1}{L_{\alpha2}L_1} & A_{4,3} & A_{4,4} & 0 & \frac{-M}{L_{\alpha2}L_1} & 0 & \frac{-1}{L_{\alpha2}} \\ \frac{1}{C_1} & 0 & 0 & 0 & 0 & \omega_0 & 0 & 0 \\ 0 & \frac{1}{C_1} & 0 & 0 & -\omega_0 & 0 & 0 & 0 \\ 0 & 0 & \frac{1}{C_2} & 0 & 0 & 0 & 0 & \omega_0 \\ 0 & 0 & 0 & \frac{1}{C_2} & 0 & 0 & -\omega_0 & 0 \end{bmatrix} \quad (10)$$

$$\boldsymbol{B} = \begin{bmatrix} \frac{1}{L_{\alpha1}} & 0 & i_{1,q,0} & B_{1,4} \\ 0 & \frac{1}{L_{\alpha1}} & -i_{1,d,0} & B_{2,4} \\ \frac{M}{L_{\alpha2}L_1} & 0 & i_{2,q,0} & B_{3,4} \\ 0 & \frac{M}{L_{\alpha2}L_1} & -i_{2,d,0} & B_{4,4} \\ 0 & 0 & v_{C1,q,0} & 0 \\ 0 & 0 & -v_{C1,d,0} & 0 \\ 0 & 0 & v_{C2,q,0} & 0 \\ 0 & 0 & -v_{C2,d,0} & 0 \end{bmatrix} \quad (11)$$

$$\boldsymbol{C} = \begin{bmatrix} v_{1,d,0} & v_{1,q,0} & 0 & 0 & 0 & 0 & 0 & 0 \\ 0 & 0 & \frac{4 \cdot i_{2,d,0} \cdot V_{dc,out,0}}{\pi\sqrt{i_{2,d,0}^2 + i_{2,q,0}^2}} & \frac{4 \cdot i_{2,q,0} \cdot V_{dc,out,0}}{\pi\sqrt{i_{2,d,0}^2 + i_{2,q,0}^2}} & 0 & 0 & 0 & 0 \end{bmatrix} \quad (12)$$

This is the accepted version of a paper published in 2019 20th Workshop on Control and Modeling for Power Electronics - COMPEL
DOI: 10.1109/COMPEL.2019.8769678

TABLE I
PARAMETERS OF SIMULATED IPT-SYSTEM

Nominal power, P_0	10 kW
Nominal operating frequency, f_0	85 kHz
Nominal coupling factor, k	0.2
Primary coil	
Nominal voltage, V_1	380 V
Self-inductance, L_1	176 μH
Quality factor, Q_1	310
Secondary coil	
Nominal voltage, V_2	235 V
Self-inductance, L_2	41 μH
Quality factor, Q_2	270

$$
\begin{aligned}
A_{2,4} = A_{1,3} &= -\frac{M}{L_{\alpha 1} L_2}\left(R_2 + \frac{4 \cdot i_{2,dq,0}^2 \cdot V_{dc,out,0}}{\pi (i_{2,d,0}^2 + i_{2,q,0}^2)^{3/2}}\right) \\
A_{1,4} = A_{2,3} &= -\frac{4 M V_{dc,out,0}}{\pi L_{\alpha 1} L_2} \frac{i_{2,d,0} \cdot i_{2,q,0}}{(i_{2,d,0}^2 + i_{2,q,0}^2)^{3/2}} \\
A_{3,3} = A_{4,4} &= -\frac{1}{L_{\alpha 2}}\left(R_2 + \frac{4 \cdot i_{2,dq,0}^2 \cdot V_{dc,out,0}}{\pi (i_{2,d,0}^2 + i_{2,q,0}^2)^{3/2}}\right) \\
A_{3,4} = A_{4,3} &= \pm\omega_0 - \frac{4 V_{dc,out,0}}{\pi L_{\alpha 2}} \frac{i_{2,d,0} \cdot i_{2,q,0}}{(i_{2,d,0}^2 + i_{2,q,0}^2)^{3/2}} \\
B_{1,4} = B_{2,4} &= -\frac{4M}{\pi L_{\alpha 1} L_2} \frac{i_{2,dq,0}}{\sqrt{i_{2,d,0}^2 + i_{2,d,0}^2}} \\
B_{3,4} = B_{3,4} &= -\frac{4}{\pi L_{\alpha 2}} \frac{i_{2,dq,0}}{\sqrt{i_{2,d,0}^2 + i_{2,q,0}^2}}
\end{aligned}
\tag{13}
$$

B. Model verification

The validity and accuracy of the nonlinear state-space model defined by (8) and the corresponding linearized model defined by (9)-(13) is validated by time-domain simulations in the MATLAB/Simulink/Simscape environment, using the parameters in Table I. As the validity of a similar model representing a system operated at its resonance frequency is demonstrated in [16], only examples with off-resonant operation are presented in the following. For the simulations shown in Fig. 6, the system is first linearized at steady-state operation in a condition close to the nominal coupling, with slightly sub-resonant frequency for maintaining nominal power transfer. A step change of 10% in the input voltage is applied at t = 2 ms, and after steady-state operation is achieved, a similar step change in the receiving side voltage is applied at t = 2.4 ms. After reaching steady-state operation with these conditions, the system is brought back to the linearization point at t = 2.8 ms. The dynamic responses of the sending and receiving side currents resulting from the circuit model in Fig. 1, the nonlinear state-space model from (8) and the corresponding linearized model, are shown in the same plots for comparison.

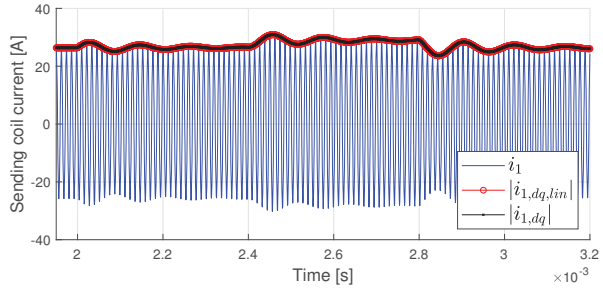

(a) Sending side currents.

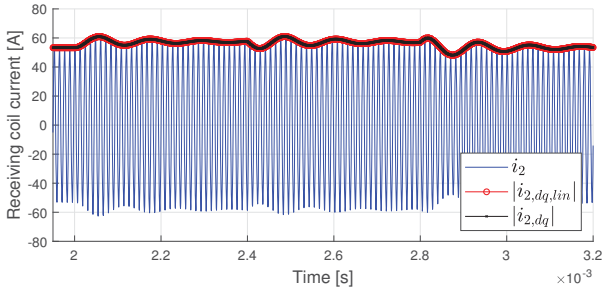

(b) Receiving side currents.

Fig. 6. Comparison of the current dynamics for the simulated models along the constant power trajectory. Simulation point $k = 1.02 k_{nom}$, $\omega = 0.988\omega_0$.

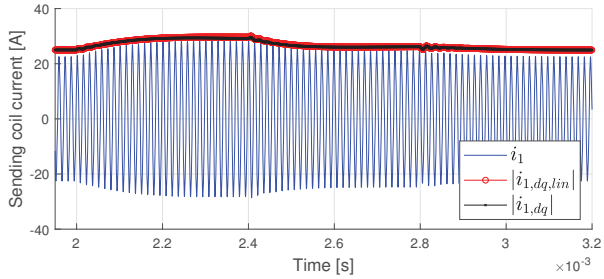

(a) Sending side currents.

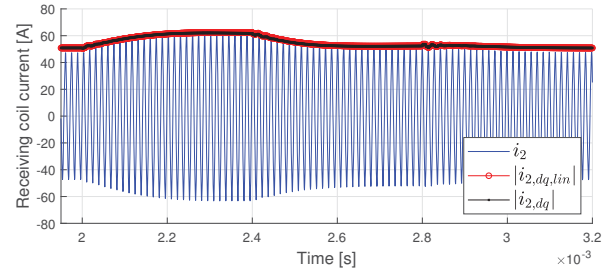

(b) Receiving side currents.

Fig. 7. Comparison of the current dynamics for the simulated models along the constant power trajectory. Simulation point $k = 2.6 k_{nom}$, $\omega = 0.827\omega_0$.

The same sequence is repeated for a relatively high coupling coefficient and a correspondingly reduced frequency in Fig. 7. The results show that both the nonlinear and linearized state-space models accurately capture the dynamics of the system along the constant power trajectory illustrated in Fig. 5.

To further document the validity of the presented state-space models, additional time-domain simulations are presented in

This is the accepted version of a paper published in 2019 20th Workshop on Control and Modeling for Power Electronics - COMPEL
DOI: 10.1109/COMPEL.2019.8769678

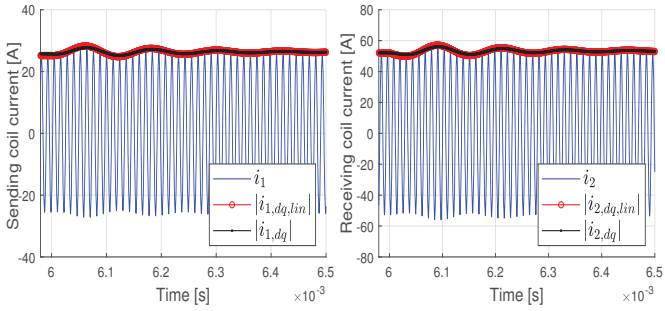

(a) (b)

Fig. 8. Comparison of the current dynamics for the simulated models along the constant power trajectory. Simulation point $k = 1.02k_{nom}$, $\omega = 0.988\omega_0$.

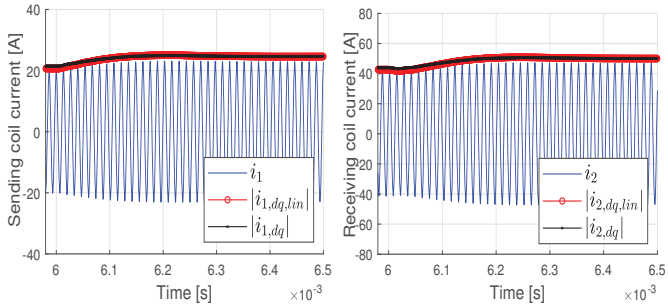

(a) (b)

Fig. 9. Comparison of the current dynamics for the simulated models along the constant power trajectory. Simulation point $k = 2k_{nom}$, $\omega = 0.866\omega_0$.

Fig. 8 and Fig. 9, illustrating how the system behaves in response to a step change in the operating frequency. For the simulations presented in Fig. 8, the small-signal model is obtained at the same operating point as in Fig. 6. The system is first at steady-state conditions with an operating frequency of 10 700 rad/s higher than the frequency where the system is linearized, before a step back to the linearization point is applied at t = 6 ms. A similar sequence is repeated in another point along the frequency trajectory in Fig. 5 and the results are shown in Fig. 9, this time with a step change of 5 350 rad/s. From 8a, a slight deviation can be observed, indicating that the accuracy of the small-signal model is sensitive to changes in the operating frequency. However, the oscillation frequency and settling time are virtually identical, demonstrating that the small-signal model provides accurate results as long as it is operated close to the linearization point.

IV. Analysis of System Dynamics and Control

The linearized model from (9)-(13) can be utilized to evaluate the small-signal dynamics of the system and to design suitable control loops for regulating the power transfer.

A. Eigenvalue analysis

The change in the eigenvalues of the $\boldsymbol{A}$-matrix when the coupling conditions are changed in the range of $k_{nom} \leq k \leq 3k_{nom}$ while ensuring constant power transfer by operating

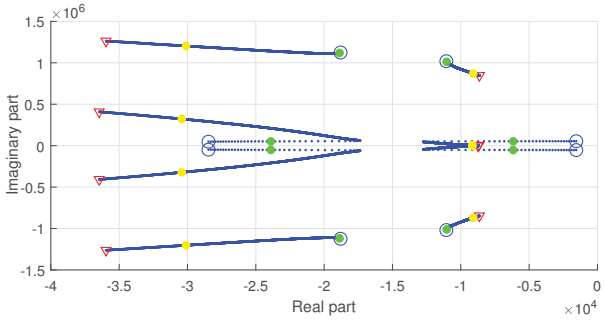

Fig. 10. Eigenvalue trajectory for variation of k in the range $k_{nom} \leq k \leq 3k_{nom}$ with frequency control for maintaining constant power: points market with blue circles correspond to $k = k_{nom}$ and points marked with red triangles corresponds to $k = 3k_{nom}$. Operating points in Fig. 6 and Fig. 7 are marked with green and yellow circles, respectively.

on the frequency trajectory from Fig. 5 is shown in Fig. 10. The figure also shows the operating points used for the time-domain simulations in Fig. 6 and Fig. 7, which are marked with green and yellow circles, respectively. As seen from the figure, the system will have a dominant pole-pair with relatively low oscillation frequency and long settling time when operating close to the nominal coupling. The corresponding oscillation mode is clearly seen in the time-domain results in Fig. 6 and Fig. 8. The real part of this dominating pole-pair rapidly decreases when the operating frequency is moved away from the resonance frequency along the trajectory from Fig. 5. However, a sudden change in the movement of these eigenvalues appears around an operating condition with coupling factor $k \approx 1.04k_{nom}$ and operating frequency $\omega \approx 0.98\omega_0$. For an increased coupling coefficient beyond this point, the imaginary part of the dominant eigenvalues decreases while the real part increases when the operating frequency is reduced, making the system more damped but slower. The corresponding differences in system dynamics for close to nominal coupling compared to high coupling conditions are also clearly seen from the simulated responses in Fig. 6 and Fig. 7 or Fig. 8 and Fig. 9, respectively.

B. Power controller design

The small-signal state-space model from (9)-(13) can also be utilized to extract the input-output frequency domain characteristics of the system and to support frequency domain design of control loops. In order to regulate the power transfer in response to variations in the coupling conditions according to the strategy defined by Fig. 4 and Fig. 5, a simple PI-controller can be utilized to change the operating frequency [9]. For explicit regulation of the power provided to the load, it would be necessary to use the received power P_{out} as the feedback signal. However, this would imply the need for feedback across the air gap of the wireless power transfer. Thus, it would be preferable to use only feedback signals from the sending side to regulate the power transfer.

Assuming power control by a PI-controller, the open loop transfer functions for control loops based on feedback from

This is the accepted version of a paper published in 2019 20th Workshop on Control and Modeling for Power Electronics - COMPEL
DOI: 10.1109/COMPEL.2019.8769678

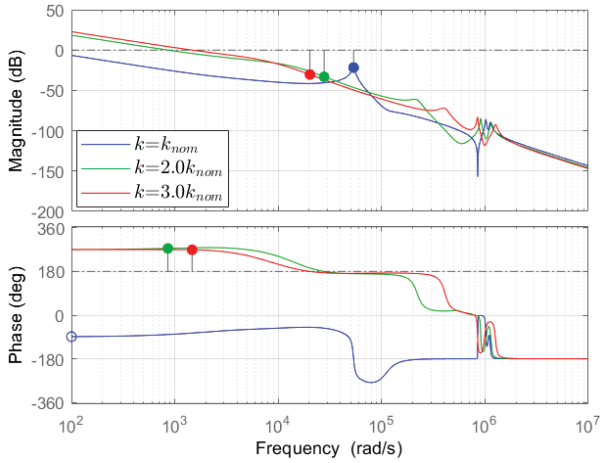

Fig. 11. Frequency response of open loop transfer function from P_{ref} to P_{in} for three different coupling conditions.

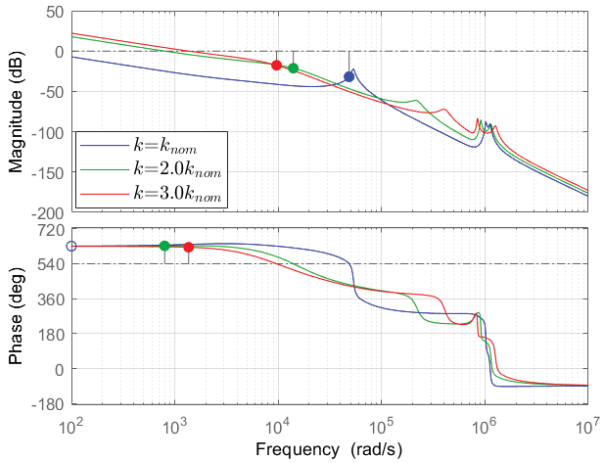

Fig. 12. Frequency response of open loop transfer function from P_{ref} to P_{out} for three different coupling conditions.

either the sending side power P_{in} or the receiving side power P_{out} can be expressed as:

$$\frac{P_{in}}{P_{ref}}(s) = h_r h_{p1} h_f(s) = k_p \frac{1+T_i s}{T_i s} h_{p1}(s) \frac{1}{1+T_f s} \quad (14)$$

$$\frac{P_{out}}{P_{ref}}(s) = h_r h_{p2} h_f(s) = k_p \frac{1+T_i s}{T_i s} h_{p2}(s) \frac{1}{1+T_f s} \quad (15)$$

In these equations, $h_{p1}(s)$ and $h_{p2}(s)$ are the transfer functions from the small-signal frequency input to P_{in} and P_{out}, respectively. Additionally, the open loop transfer functions include the assumed PI-controller $h_r(s)$ and a low-pass filter $h_f(s)$ with time constant $T_f = 100/2\pi f_0$ for extracting the average value of the single-phase power flow. The frequency characteristics of the two open loop transfer functions in (14) and (15) are shown for three different coupling conditions in Fig. 11 and Fig. 12, respectively.

In order to achieve robust closed-loop performance over the whole variation range $k_{nom} \leq k \leq 3k_{nom}$, the general

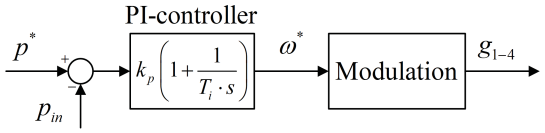

Fig. 13. Power controller for off-resonant operation by sending side feedback.

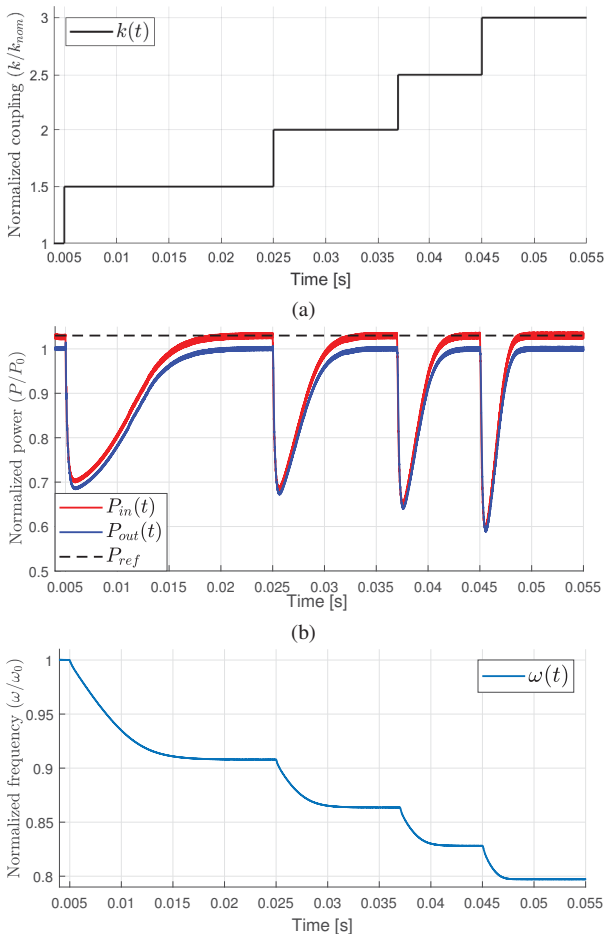

Fig. 14. Closed-loop response to step changes in coupling factor with feedback of sending side power. The sending side power reference is adjusted to compensate for the efficiency of the system.

frequency characteristics in Fig. 11 and Fig. 12 are utilized to design the PI-controller parameters such that no overshoot or oscillations occur at operating conditions where the system dynamics are fast. The resulting parameters are selected to be $k_p = -0.65057$ and $T_i = 1/2846$, and the corresponding amplitude- and phase-margins with the different feedback signals are indicated in Fig. 11 and Fig. 12. However, the design for damped response in all coupling conditions implies a relative slow response close to the nominal coupling.

To illustrate the performance when using only sending side power feedback for the control, results from operating the system with the simple control loop in Fig. 13 is shown in Fig. 14. The sequence of ideal steps applied in the coupling factor is shown in Fig. 14a while Fig. 14b shows the resulting

This is the accepted version of a paper published in 2019 20th Workshop on Control and Modeling for Power Electronics - COMPEL
DOI: 10.1109/COMPEL.2019.8769678

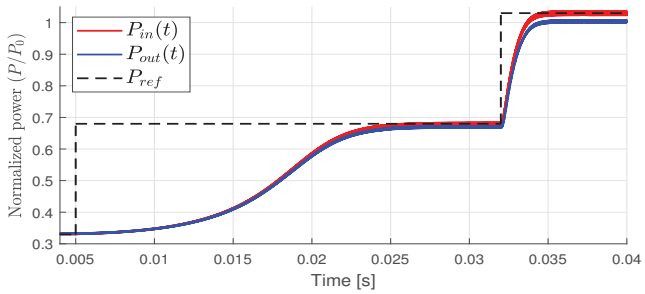

(a)

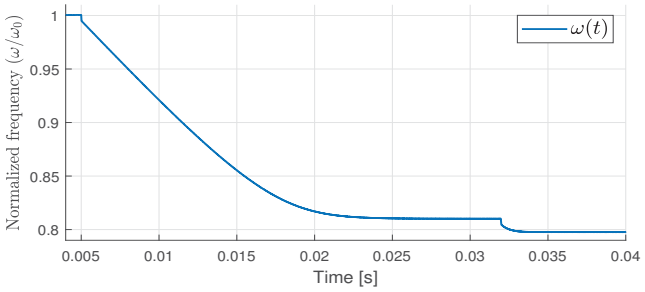

(b)

Fig. 15. Response to steps in the power reference with control based only on sending side feedback.

output power. As indicated by the figure, the power reference is increased slightly above 1.0 to compensate for the losses in the system. The operating frequency resulting as output from the PI-controller in Fig. 13 is shown in Fig. 14c. As can be seen, the response is much faster in the case of high coupling coefficient, which is expected when considering the frequency trajectory in Fig. 5 and the frequency characteristics in Fig. 12. The results also confirm how the operating frequency resulting from the closed-loop controller corresponds to the trajectory for maintaining nominal power according to 5.

Another example of the closed-loop power control performance is shown in Fig. 15. In this case, the system is initially operating at the secondary side resonance frequency according to the red curve in Fig. 4a with $k = 3k_{knom}$ and a correspondingly low power reference of 0.32 pu. A step in the sending side power reference to 0.66 pu is applied at t = 5 ms, and a second step in the power reference is applied at t = 32 ms, bringing the system to the operating point corresponding to nominal power transfer indicated by the red circle in Fig. 4a. The operating frequency resulting from the PI-controller is shown in Fig. 15b. The results clearly illustrate how the response is stable and well damped over the entire operating region, although much faster when approaching operation at rated power at high coupling.

V. Conclusion

This paper has presented a time-invariant state-space model of a Series-Series (SS) compensated Inductive Power Transfer (IPT) system designed for battery charging with minimized component ratings. The evaluated system is intended for power flow control by off-resonant operation during variations in the coupling conditions, which is obtained by utilizing the bifurcated characteristics of the IPT system to allow for frequency control with constant input and output voltages. The presented model accurately represents the influence of the Constant Voltage Load (CVL) characteristics resulting from a receiving side diode rectifier directly interfaced to the battery. The linearized state-space model is utilized to evaluate the small-signal dynamics over the full range of expected operating conditions. This small-signal analysis is also utilized to design a simple but robust PI-controller, which can operate with only sending side feedback for regulating the power flow in response to variations in the coupling conditions.

References

[1] C. T. Rim and C. Mi, *Wireless power transfer for electric vehicles and mobile devices*. John Wiley & Sons, 2017.

[2] G. A. Covic and J. T. Boys, "Modern trends in inductive power transfer for transportation applications," *IEEE Journal of Emerging and Selected topics in power electronics*, vol. 1, no. 1, pp. 28–41, 2013.

[3] S. Li and C. C. Mi, "Wireless power transfer for electric vehicle applications," *IEEE journal of emerging and selected topics in power electronics*, vol. 3, no. 1, pp. 4–17, 2014.

[4] "Wireless power transfer for light-duty plug-in/electric vehicles and alignment methodology," SAE Recommended Practice, International J2954 Taskforce, 2019.

[5] R. Bosshard, U. Badstübner, J. W. Kolar, and I. Stevanović, "Comparative evaluation of control methods for inductive power transfer," in *2012 International Conference on Renewable Energy Research and Applications (ICRERA)*. IEEE, 2012, pp. 1–6.

[6] Z. Yan, Y. Zhang, T. Kan, F. Lu, K. Zhang, B. Song, and C. C. Mi, "Frequency optimization of a loosely coupled underwater wireless power transfer system considering eddy current loss," *IEEE Transactions on Industrial Electronics*, vol. 66, no. 5, pp. 3468–3476, 2019.

[7] G. Guidi and J. A. Suul, "Minimization of converter ratings for mw-scale inductive charger operated under widely variable coupling conditions," in *2015 IEEE PELS Workshop on Emerging Technologies: Wireless Power (2015 WoW)*. IEEE, 2015, pp. 1–7.

[8] G. Guidi, J. A. Suul, F. Jenset, and I. Sorfonn, "Wireless charging for ships: high-power inductive charging for battery electric and plug-in hybrid vessels," *IEEE Electr. Mag.*, vol. 5, no. 3, pp. 22–32, 2017.

[9] G. Guidi, "An apparatus and a method for wireless transmission of power between dc voltage sources," Norwegian Patent, Jan. 2015.

[10] G. Guidi and J. A. Suul, "Minimizing converter requirements of inductive power transfer systems with constant voltage load and variable coupling conditions," *IEEE Transactions on Industrial Electronics*, vol. 63, no. 11, pp. 6835–6844, Nov 2016.

[11] S. R. Sanders, J. M. Noworolski, X. Z. Liu, and G. C. Verghese, ""Generalized averaging method for power conversion circuits"," *IEEE Trans. on Power Electron.*, vol. 6, no. 2, pp. 251–259, April 1991.

[12] Z. U. Zahid, Z. M. Dalala, C. Zheng, R. Chen, W. E. Faraci, J. J. Lai, G. Lisi, and D. Anderson, "Modeling and control of seriesseries compensated inductive power transfer system," *IEEE J. of Emerg. and Sel. Topics in Power Electron.*, vol. 3, no. 1, pp. 111–123, March 2015.

[13] D. Gunji, T. Imura, and H. Fujimoto, "Envelope model of load voltage on series-series compensated wireless power transfer via magnetic resonance coupling," in *2015 IEEE PELS Workshop on Emerging Technologies: Wireless Power (2015 WoW)*, June 2015, pp. 1–6.

[14] K. Song, C. Zhu, K. Koh, D. Kobayashi, T. Imura, and Y. Hori, "Modeling and design of dynamic wireless power transfer system for ev applications," in *IECON 2015 - 41st Annual Conference of the IEEE Industrial Electronics Society*, Nov 2015, pp. 005 229–005 234.

[15] R. Tavakoli and Z. Pantic, "Analysis, design, and demonstration of a 25-kw dynamic wireless charging system for roadway electric vehicles," *IEEE Journal of Emerging and Selected Topics in Power Electronics*, vol. 6, no. 3, pp. 1378–1393, Sep. 2018.

[16] G. Guidi and J. A. Suul, ""Modelling techniques for designing high-performance on-road dynamic charging systems for electric vehicles"," in *Proc. 31st Int. Electric Vehicle Symposium and Exhibition & Int Electric Vehicle Technology Conf.*, 09 2018, pp. 1–7.

This is the accepted version of a paper published in 2019 20th Workshop on Control and Modeling for Power Electronics - COMPEL
DOI: 10.1109/COMPEL.2019.8769678